Journal of Alloys and Compounds 499 (2010) 259–264

Contents lists available at ScienceDirect

Journal of Alloys and Compounds

journal homepage: www.elsevier.com/locate/jallcom

In-situ hydrothermal synthesis of three-dimensional MnO_2–CNT nanocomposites and their electrochemical properties

Fei Teng[a], Sunand Santhanagopalan[a], Ying Wang[b], Dennis Desheng Meng[a,*]

[a] *Department of Mechanical Engineering-Engineering Mechanics, Michigan Technological University, Houghton, MI 49931, USA*
[b] *Department of Mechanical Engineering, Louisiana State University, Baton Rouge, LA 70803, USA*

ARTICLE INFO

Article history:
Received 16 December 2009
Received in revised form 19 March 2010
Accepted 19 March 2010
Available online 27 March 2010

Keywords:
Three-dimensional nanostructure
MnO_2–CNT nanocomposite
In-situ
Hydrothermal
Supercapacitor

ABSTRACT

Three-dimensional (3-D) MnO_2–carbon nanotube (CNT) nanocomposites were prepared by a simple one-pot hydrothermal method. An electrode was then prepared with these nanocomposites. For comparative investigation, MnO_2 microspheres were also hydrothermally prepared without adding CNTs. The as-synthesized MnO_2 microspheres were then mechanically mixed with CNTs to prepare a subsequent electrode. The samples were characterized by electron microscopy, X-ray diffraction, and electrochemical methods. It has been revealed that a 3-D conductive network of CNTs was formed with microspheres of MnO_2 nanorods interwoven with and connected by CNTs. As a result, the hydrothermally mixed MnO_2–CNT electrode showed a higher specific capacitance than the mechanically mixed electrode. It has therefore been concluded that the hydrothermal mixing method yields a more homogeneous product that is better suited to take full advantages of both the high capacitance of MnO_2 and the high electrical conductivity of CNTs. The 3-D MnO_2–CNT nanocomposites reported herein have provided a promising electrode material for supercapacitors and other electrochemical energy storage/conversion devices.

1. Introduction

Recently, supercapacitors [1] have attracted intensive research interest due to their capability to deliver very high power density, which makes them indispensable candidates as power boosters for hybrid electric vehicles, mobile electronic devices, distributed sensor networks, and so on. The chemical energy of a supercapacitor is stored in the electrical double-layer (EDL) between the electrode and the electrolyte [2]. The fast, non-Faradayic discharge of the EDL enables supercapacitors to deliver very high power density. Moreover, the energy density or capacitance of an electrochemical supercapacitor can be significantly improved by introducing pseudocapacity. MnO_2 is among the most promising pseudocapacitor electrode materials due to its large specific capacitance, environmentally benign nature, and cost effectiveness [3–7]. Nevertheless, a major drawback of MnO_2 is its poor electrical conductivity, which limits its power-delivery capability. An effective approach to overcome this disadvantage is the introduction of electronically conductive materials, such as graphite [8], carbon nanofibers [9] and CNTs [3,10–29]. Among them, CNTs have been intensively investigated for their excellent conductivity, large intrinsic area, and chemical stability. CNTs are also reported to form well-controlled microstructures with MnO_2 for supercapacitor applications, such as MnO_2 nanowires on CNT paper [30], coaxial MnO_2–CNT arrays [31], and MnO_2 nanoflowers on vertically aligned CNT arrays [32]. It has been demonstrated that the electrochemical performances of electrodes can be significantly improved by employing MnO_2–CNT composite structures. In these composite structures, the large interfacial area between MnO_2 and electrolyte can enhance the electrochemical utilization of MnO_2 in the nanocomposites. The increased contact area between MnO_2 and CNTs, as well as their intimate bonding, is also desirable for the improvement of the electrical conductivity of the nanocomposite electrode due to the intrinsic high conductivity of CNTs [33,34]. It has been reported that the nanocomposite microstructure has an important influence on their electrochemical properties. To ensure optimal electrochemical performance, it is very important to obtain MnO_2 nanoparticles uniformly distributed on a conductive network of CNTs. The contact resistance between MnO_2 and CNTs should also be minimized by intimately bonding them together. Such characteristics in the microstructures of MnO_2–CNT nanocomposites obviously take root in the methods that are employed to prepare them, which can be classified into physical/mechanical-mixing [35,36] and chemical/electrochemical deposition [19–25]. It is therefore desirable to effectively synthesize nanocomposites with the above-mentioned optimal structural characteristics with a simple method.

In this work, a novel 3-D MnO_2–CNT nanocomposite was prepared by a simple one-pot hydrothermal method. The process resulted in a highly porous structure of a conductive CNT network

* Corresponding author. Tel.: +1 906 487 3551; fax: +1 906 487 3551.
E-mail address: dmeng@mtu.edu (D.D. Meng).

0925-8388/$ – see front matter © 2010 Elsevier B.V. All rights reserved.
doi:10.1016/j.jallcom.2010.03.181

uniformly filled and interwoven with highly dispersed, hierarchical microspheres consisting of MnO_2 nanorods. The CNTs and MnO_2 nanorods can be intimately bonded to each other, so as to render the following distinct characteristics to the 3-D MnO_2–CNT nanocomposites: (i) the improved electrical conductivity due to the presence of the CNT conductive network; (ii) the enhanced electrochemical accessibility of electrolyte due to the porous electrode structure. Such a homogeneous, hybrid microstructure can take advantage of the excellent intrinsic properties of both MnO_2 and CNTs. The samples were characterized by field-emission scanning electron microscopy (FE-SEM), high-resolution transmission electron microscopy (HRTEM), electron diffraction (ED), X-ray energy dispersive spectroscopy (EDX) and X-ray diffractometry (XRD). The capacitive behaviors of the 3-D MnO_2–CNT nanocomposite electrode were investigated and compared to those of a mechanically mixed composite electrode. The comparative study was also carried out to reveal the impact of preparation methods on the microstructures and electrochemical properties of nanocomposite electrodes.

2. Experimental

2.1. Chemicals

The deionized water used in this work was prepared in house with a Thermo Scientific D4521 B-pure deionization system. All other chemicals were of analytical grade and used as received. Multi-wall carbon nanotubes (CNTs) were purchased from MER Corporation. $MnSO_4{\cdot}H_2O$, $(NH_4)_2S_2O_8$, Na_2SO_4, polytetrafluoroethylene (PTFE) and *N*-methyl-2-pyrrolidone were purchased from Sigma–Aldrich.

2.2. Preparation of the samples

The 3-D MnO_2–CNT nanocomposites were prepared by an *in-situ* hydrothermal method. Specifically, 0.025 g of CNTs was added to a 35 mL aqueous solution containing 0.02 g of $MnSO_4{\cdot}H_2O$ and 0.026 g of $(NH_4)_2S_2O_8$. The mixture was stirred for 2 h to form a stable suspension, and then loaded into a Teflon®-lined stainless-steel autoclave (capacity: 50 mL). The autoclave was heated to 90 °C and kept at this temperature for 24 h. The autoclave was then naturally cooled to room temperature. The black precipitate was separated by centrifugation, and then washed with water and ethanol three times. After that, the recovered product was dried at 80 °C in a vacuum oven for 24 h. The weight percentage of CNTs in the MnO_2–CNT sample is calculated to be 5 wt%. For comparison, γ-MnO_2 microspheres were prepared by a similar procedure without adding CNTs.

2.3. Characterization

Scanning electron microscopy (SEM) images were taken by using a Hitachi S-4700 field-emission scanning electron microscopy (FE-SEM). The FE-SEM samples were coated with a 5-nm thin layer of platinum/chromium using DC sputtering. The acceleration voltage was 15 keV and the acceleration current was 1.2 nA. The morphology, structure, and composition of the samples were determined by high-resolution transmission electron microscopy (HRTEM, JEOL JEM-4000FX) equipped with electron diffraction energy dispersive X-ray spectroscopy (EDX) at an acceleration voltage of 200 kV. The powders were ultrasonically dispersed in ethanol, and then deposited on a thin amorphous carbon film supported by a copper grid. The crystal structures of the samples were characterized by X-ray powder diffractometer (XRD, Rigaku D/MAX-RB), using graphite monochromatized Cu K_α radiation (λ = 0.154 nm), operating at 40 kV and 50 mA. The XRD patterns were obtained in the range of 10–70° (2θ) at a scanning rate of 5° min^{-1}.

2.4. Electrode fabrication and electrochemical characterization

The fabrication processes of the electrodes are described as follows: the hydrothermally synthesized MnO_2–CNT powder (95 wt%) was mixed with PTFE (5 wt%) in an agate mortar. The mixture was then ground sufficiently to ensure good homogeneity, wherein *N*-methyl-2-pyrrolidone was used as solvent. The resultant slurry was cast onto the pre-cleaned stainless-steel plate. The electrode was air-dried overnight and then dried at 80 °C in a vacuum oven for 24 h. The as-prepared electrode was designated as HE. The loading was determined by a weighing method. For comparison, γ-MnO_2 nanorod microspheres (95 wt%) were mechanically mixed with CNTs (5 wt%) in an agate mortar, and the mixture was then ground sufficiently to ensure homogeneity. Finally, this mixture (95 wt%) was mixed with PTFE (5 wt%), wherein *N*-methyl-2-pyrrolidone was used as solvent. The electrode was prepared with the same procedures as mentioned above and designated as ME.

Cyclic voltammetry and galvanostatic charge–discharge measurements were performed using a potentiostat/galvanostat (Princeton Applied Research P/G, V4) with a three-electrode configuration. Pt wire and Ag/AgCl (saturated KCl, 0.222 V vs. standard hydrogen electrode) were employed as the counter and reference electrodes, respectively. Prior to testing, 0.5 M Na_2SO_4 solutions were purged with N_2 for 0.5 h and then used as the electrolyte. Cyclic voltammetry was performed in the potential range of 0.1–0.8 V at different scanning rates. The chronopotential test was performed in the potential range of 0–1 V at a current density of 1 mA cm^{-2}.

3. Results and discussion

3.1. Microstructures and crystal structures of the samples

Fig. 1 shows the FE-SEM micrographs of the as-synthesized samples. Fig. 1a demonstrates the uniform microspheres with an average size of about 5 μm, observed in the as-synthesized MnO_2 sample without adding CNTs. At a higher magnification (Fig. 1b), these microspheres show hierarchical structures consisting of nanorods with a diameter of about 30 nm and a length of about 1 μm. The as-synthesized MnO_2–CNT nanocomposites are shown in Fig. 1c–e. Observed from Fig. 1c, the sample is composed of 5-μm MnO_2 microspheres that are connected together by CNTs. At a higher magnification (Fig. 1d), it can be observed that some MnO_2 nanorods have been directly deposited on the surface of the CNTs. It is also noticed that the microspheres are evenly distributed in the network of CNTs. The hierarchical structure of a microsphere is again observed with CNTs interwoven within them (Fig. 1e). It is hypothesized that the negative MnO_4^- ions could be adsorbed onto the positively charged CNT surface by electrostatic attraction [37]. Under hydrothermal conditions, the redox reaction between Mn^{2+} and MnO_4^- may take place on the CNT surface [25,28]. Therefore, MnO_2 can grow on the CNT surface and eventually lead to the interweaving 3-D structure of CNTs and microspheres. The highly porous 3-D structure with nanotube/nanowire components can shorten the diffusion path for charge-carrier ions, while the large liquid–solid interface facilitates ion exchange between the electrode and electrolyte. Moreover, the uniformly embedded electronic conducting network can improve the high-rate capability as well as the specific capacitance of the materials [38].

The MnO_2–CNT nanocomposites are also characterized by HRTEM. Fig. 2a shows the formation of MnO_2 nanorods in the MnO_2–CNT nanocomposites. The ED patterns in Fig. 2b reveal the single-crystalline nature of the MnO_2 nanorods. Fig. 2c shows a typical ED pattern of CNTs. The lattice fringe with a *d*-spacing of 0.34 nm in Fig. 2d corresponds to the (1 1 1) plane of CNTs. The element compositions of the sample are also inspected by EDX, with results shown in Fig. 2f. It is noted that the peaks of copper are caused by the copper grid, which is used as a holder.

The samples were further characterized by XRD. Fig. 3a shows the XRD patterns of the CNTs, the diffraction peak at a 2θ value of 26° was ascribed to the typical (0 0 2) reflection of CNTs [11,39,40]. Fig. 3b shows the XRD patterns of the 3-D MnO_2–CNT nanocomposites. In addition to a very weak (0 0 2) diffraction peak of CNTs, all the other peaks can be indexed to the γ-MnO_2 (JCPDS no. 14-0644), indicating the formation of γ-MnO_2–CNT nanocomposites. Fig. 3c shows the XRD patterns of the sample prepared without adding CNTs, confirming the formation of pure γ-MnO_2 crystals.

3.2. Electrochemical properties of the electrodes

Fig. 4a shows the typical cyclic voltammograms (CVs) of the HE electrode at different scanning rates in a potential range of 0.1–0.8 V. The nearly rectangular shape of the CVs verifies the characteristics of a nearly ideal supercapacitor. It can also be observed that the current density gradually increases with the scanning rate. This indicates that the electrolyte ions can sufficiently contact the active electrode materials. It is well known that the power characteristics of an electrode material strongly depend on the electrochemical kinetics of the redox reaction. Since the capaci-

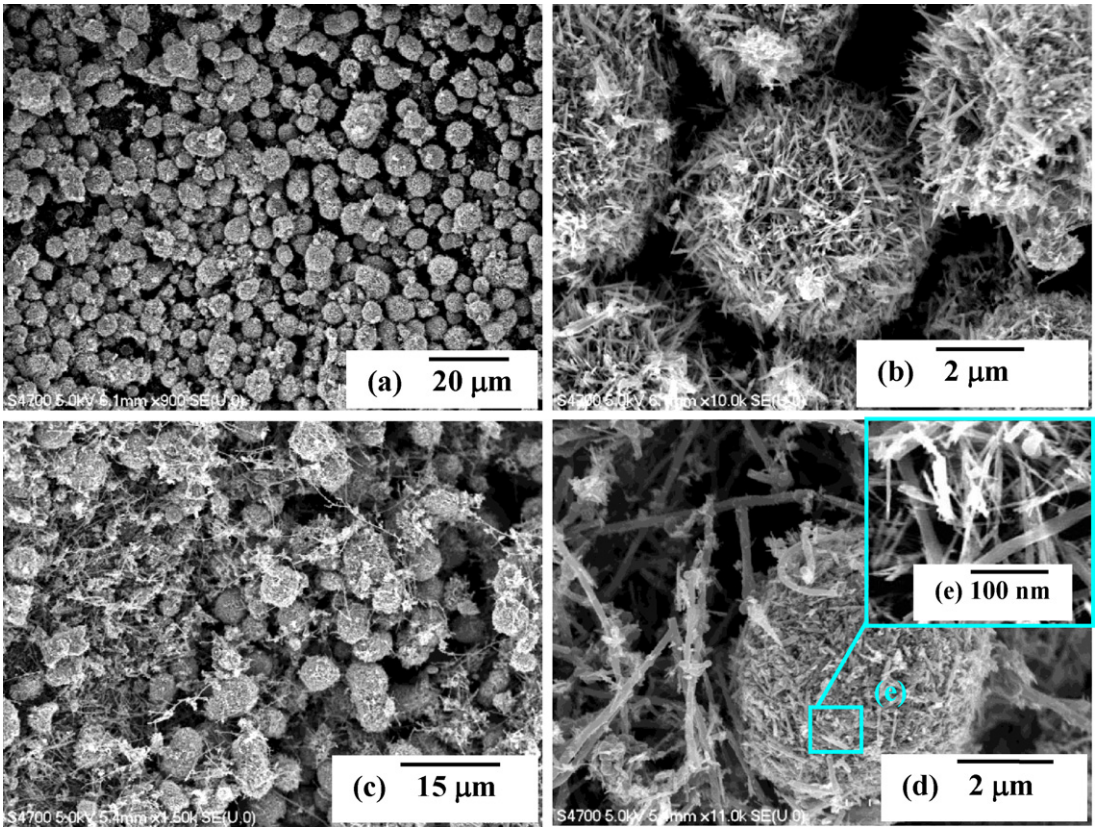

Fig. 1. FE-SEM micrographs of the samples: (a and b) MnO_2 microspheres; (c–e) MnO_2–CNT nanocomposites.

tive current response of the electrodes is mainly contributed by the redox reaction of MnO_2, it can be presumed that the 3-D network structure of the HE electrode can significantly facilitate the penetration of protons or other cations into the whole electrode matrix [21,29,41]. The specific capacitance (C_s, $F\,g^{-1}$) of the electrode was calculated from the CVs according to the following equation [42]:

$$C_s = \frac{i}{(v \times m)} \quad (1)$$

where i is the current density (A) in the CV anodic branch; v is the scanning rate ($V\,s^{-1}$) and m is the mass of active material on the electrode. Herein, C_s values were calculated and compared using the anodic branch current at 0.5 V and the total loading mass of MnO_2 and CNTs on the electrode. At a scanning rate of $5\,mV\,s^{-1}$, the specific capacitance of the HE electrode was calculated as $292\,F\,g^{-1}$. When the scanning rate was increased to 10 and $20\,mV\,s^{-1}$, the specific capacitance decreased to 274 and $255\,F\,g^{-1}$, respectively. Fig. 4b shows the CVs of the ME electrode at different scanning rates. At 5 and $10\,mV\,s^{-1}$, the CVs show nearly rectangular shape representing the redox characteristics of a nearly ideal supercapacitor. However, at a higher scanning rate (e.g., $20\,mV\,s^{-1}$), the CV curve deviates significantly from the rectangular shape. It is well known that the scanning rate has a direct influence on the diffusion of Na^+ ions. At higher scanning rates, the Na^+ ions can only reach the outer surface of the electrode. As a result, the capacitance decreases. Because the ME electrode suffers from a higher polarization resistance, the CVs of the electrode are distorted and display the delayed current reversals at both ends of the potential limits. According to the CV curves, the specific capacitance of the ME electrode was calculated as $214\,F\,g^{-1}$ at a scanning rate of $5\,mV\,s^{-1}$. When the scanning rate was increased to 10 and $20\,mV\,s^{-1}$, the specific capacitances decreased to 181 and $152\,F\,g^{-1}$, respectively. It is obvious that the HE electrode has far better electrochemical reversibility than the ME electrode. The desirable high-rate capacitive behavior of the HE electrode is mainly attributed to its high electric conductivity. It appears that the high electric conductivity of the CNTs in the HE electrode facilitates the energy extraction from MnO_2, resulting in a higher capacitance [43]. The homogeneously dispersed CNTs in the HE electrode can also alleviate the stress caused by the cycling, because of their excellent mechanical and resiliency properties [44]. As for the ME electrode, the homogeneity achieved by the mechanical-mixing method is relatively low, resulting in a relatively poor electrochemical performance.

The charge–discharge properties of the electrodes were also investigated by chronopotentiometry with the results shown in Fig. 5. The discharge capacitance of the electrode can also be evaluated from the galvanostatic charge–discharge curve according to the following equation [44]:

$$C_s = \frac{Q}{(\Delta V \times m)} = \frac{(i \times t)}{(\Delta V \times m)} \quad (2)$$

where i is the discharge current, t is the discharge time, ΔV is the potential window, m is the mass of the active materials. The C_s values for the HE and ME electrodes are calculated as 264 and $211\,F\,g^{-1}$, respectively. The higher capacitance of the HE electrode is again attributed to its homogeneous hybrid nanostructure.

The good capacitive behavior of the HE electrode can be ascribed to its high electrical conductivity and sufficient contact between active material and electrolyte solution [24]. Two mechanisms have been proposed to explain the charge storage behavior of MnO_2. The first mechanism involves the intercalation of protons (H^+) or alkali metal cations (C^+) into active material upon reduction and their deintercalation upon oxidation [45]:

$$MnO_2 + H^+ + e^- \rightarrow MnOOH \quad (3)$$

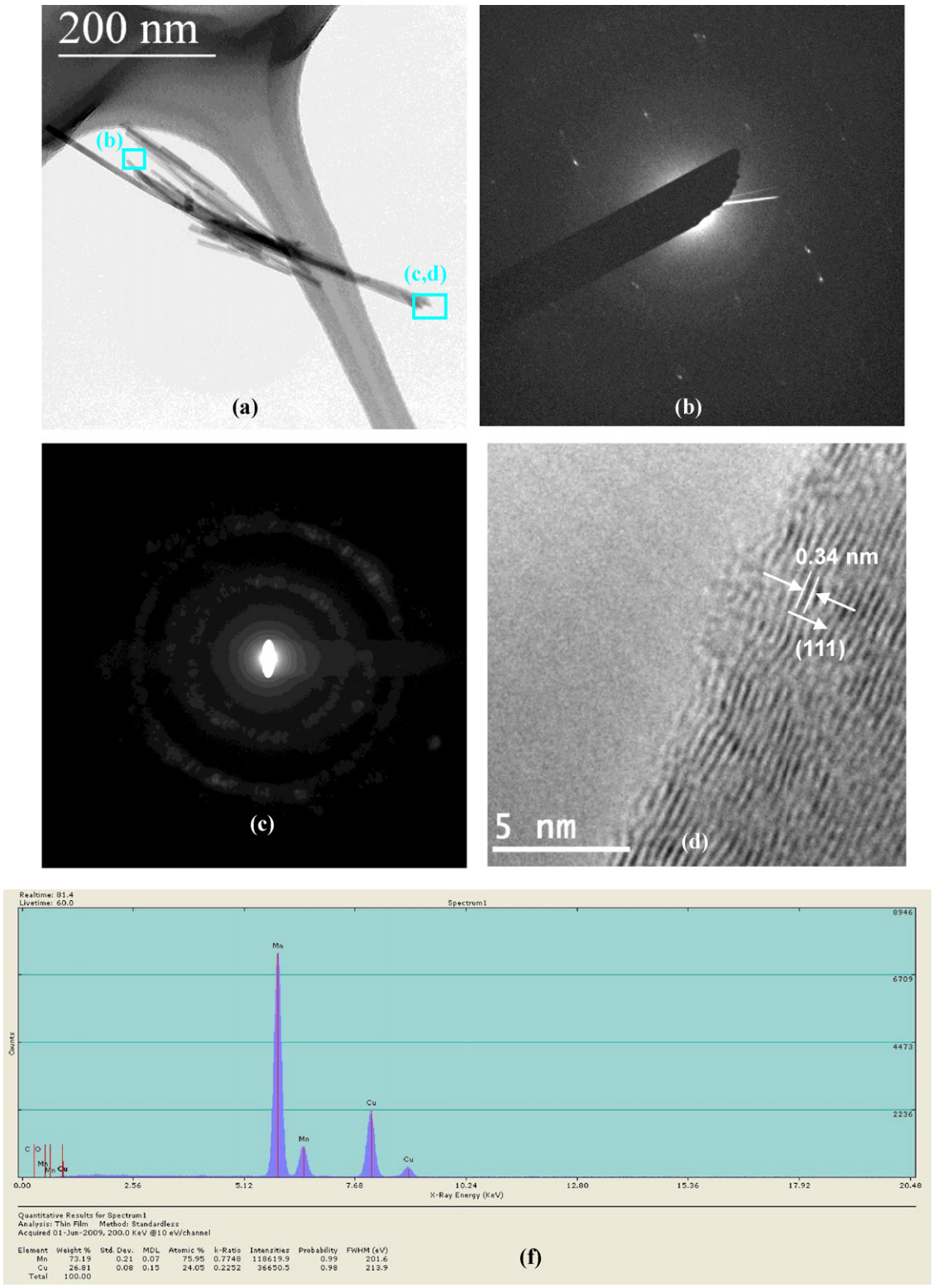

Fig. 2. HRTEM images of the MnO_2–CNT nanocomposites: (a) TEM image; (b) ED patterns of MnO_2; (c) ED patterns of CNT; (d) Lattice fringe of CNT; (e) EDX spectra of the MnO_2–CNT nanocomposites.

or

$$MnO_2 + C^+ + e^- \rightarrow MnOOC \quad (4)$$

The second mechanism is based on the surface adsorption of electrolyte cations (C^+) on MnO_2 [46,47]:

$$(MnO_2)_{surface} + (C^+) + e^- \rightarrow (MnO_2{}^-C^+)_{surface} \quad (5)$$

where $C^+ = Na^+, K^+, Li^+$.

In our study, both mechanisms seem to effectively contribute to the capacitive behavior. First of all, the electric conductivity of the HE electrode is significantly enhanced by the high homogene-

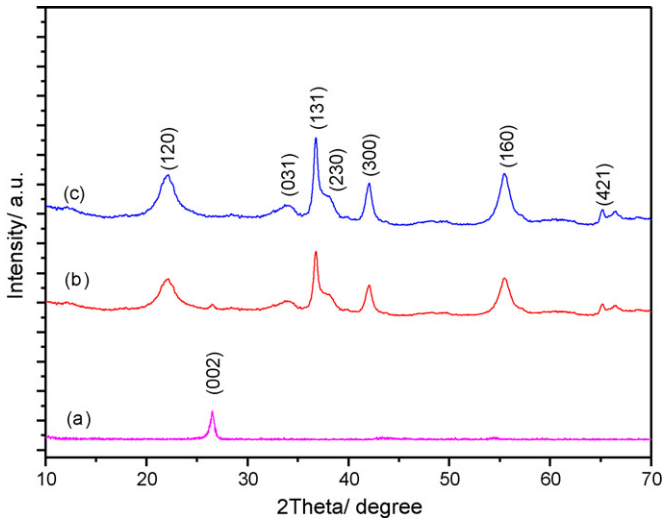

Fig. 3. X-ray diffraction patterns of the samples: (a) CNTs; (b) MnO_2–CNT nanocomposites; (c) MnO_2 microspheres.

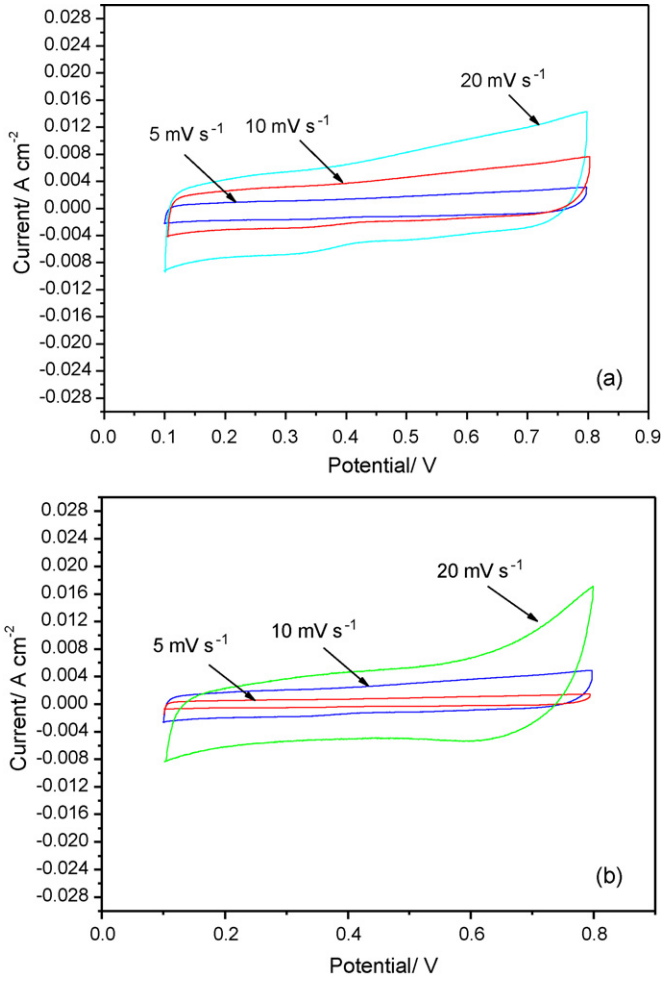

Fig. 4. Cyclic voltammograms of the as-fabricated electrodes at different scanning rates: (a) HE electrode, fabricated by the hydrothermally synthesized MnO_2–CNT nanocomposites; (b) ME electrode, fabricated by the mechanically mixed MnO_2–CNT composites.

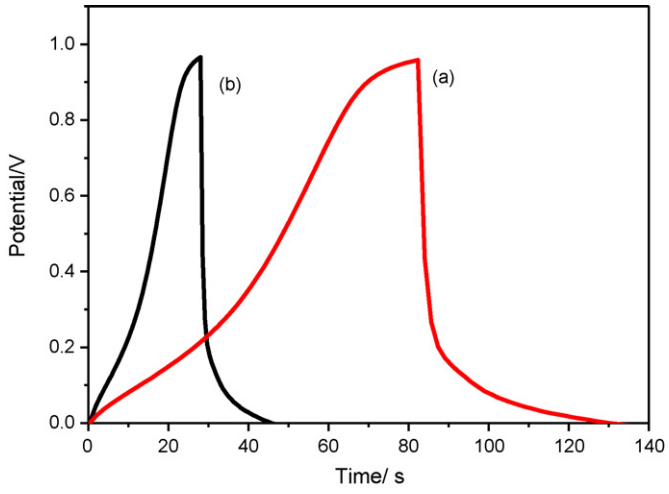

Fig. 5. Chronopotentiograms of the electrodes in 0.5 M Na_2SO_4 aqueous solution at a current density of 1 mA cm^{-2}: (a) HE; (b) ME.

ity of the nanocomposites. This facilitates the energy extraction from MnO_2, resulting in a higher capacitance [48]. The conductivities of the HE and ME electrodes are determined to be 7.1×10^{-2} and 1.0×10^{-2} S cm^{-1}, respectively, much higher than that of pure MnO_2 (10^{-6} to 10^{-3} S cm^{-1}). The reported mechanical-mixing method is not enough to achieve the high homogeneity for MnO_2 nanorod microspheres and the interweaving structure with CNTs. The poor conductivity of MnO_2 thus leads to high polarization of the electrode, which results in non-rectangular CV curves [43]. Reddy et al. [31] have reported that the excellent cyclic stability and capacitance of the MnO_2–CNT coaxial nanotube electrodes result from the hybrid nature of the electrodes with improved electric conductivity and the dual mechanism of charge storage. They concluded that the highly conductive CNT cores not only offer electron transportation capability to the MnO_2 shell, but also act as a buffer to alleviate the volume expansion. Moreover, the CNTs can provide additional sites for (C^+) storage, which leads to an enhanced reversible capacity for the electrode. Besides the above-mentioned factors, the 3-D nanoporous structure of the HE electrode in our study can provide a much large interface between active electrode material and the electrolyte. Such an effect can significantly improve the electron transportation through the conductive CNT network and the ionic transportation within the nanopores [35]. As a result, the specific capacitance of the hydrothermally mixed electrode is considerably improved. The 3-D MnO_2–CNT nanocomposites provide a promising electrode material for supercapacitors and other electrochemical energy storage/conversion devices.

4. Conclusions

3-D MnO_2–CNT nanocomposites were successfully prepared by a simple *in-situ* hydrothermal method. Compared with the method that involves mechanical-mixing, the *in-situ* hydrothermal synthesis yields a nanocomposite better suited for taking full advantage of the pseudocapacitance of MnO_2 and the high electron conductivity of CNTs, owing to its highly porous, interwoven, and homogeneous nanostructure. As a result, the hydrothermally mixed MnO_2–CNT nanocomposite electrode shows better capacitive performances than the mechanically mixed counterpart.

Acknowledgments

This work is financially supported by the Michigan Tech Faculty Startup Fund and National Science Foundation of China

(NSFC20944004). The authors would like to thank Mr. Ryan Lemmens for editorial assistance.

References

[1] B.E. Conway, Electrochemical Supercapacitors, Scientific Fundamentals and Technological Applications, Kluwer academic/Plenum press, New York, 1999.
[2] K.H. An, W.S. Kim, Y.S. Park, Y.C. Choi, S.M. Lee, D.C. Chung, D.J. Bae, S.C. Lim, Y.H. Lee, Adv. Mater. 13 (2001) 497.
[3] V. Subramanian, H.W. Zhu, B.Q. Wei, Electrochem. Commun. 8 (2006) 827.
[4] H. Adelkhani, M. Ghaemi, J. Alloys Compd. 493 (2010) 175.
[5] A. Taguchi, S. Inoue, S. Akamaru, M. Hara, K. Watanabe, T. Abe, J. Alloys Compd. 414 (2006) 137.
[6] H.-E. Wang, Z. Lu, D. Qian, S. Fang, J. Zhang, J. Alloys Compd. 466 (2008) 250.
[7] Y. Chen, C. Liu, F. Li, H.-M. Cheng, J. Alloys Compd. 397 (2005) 282.
[8] Y.-J. Yang, E.-H. Liu, L.-M. Li, Z.-Z. Huang, H.-J. Shen, X.-X. Xiang, J. Alloys Compd. 487 (2009) 564.
[9] J. Li, E.-H. Liu, W. Li, X.-Y. Meng, S.-T. Tan, J. Alloys Compd. 478 (2009) 371.
[10] R.K. Sharma, A. Karakoti, S. Seala, L. Zhai, J. Power Sources 195 (2010) 1256.
[11] C. Yuan, L. Su, B. Gao, X. Zhang, Electrochim. Acta 53 (2008) 7039.
[12] X. Huang, C. Pan, X. Huang, Mater. Lett. 61 (2007) 934.
[13] K.C. Ng, S. Zhang, C. Peng, G.Z. Chen, J. Electrochem. Soc. 156 (2009) A846.
[14] A.L.M. Reddy, M.M. Shaijumon, S.R. Gowda, P.M. Ajayan, J. Phys. Chem. C 114 (2010) 658.
[15] Z. Fan, J. Chen, B. Zhang, B. Liu, X. Zhong, Y. Kuang, Diam. Relat. Mater. 17 (2008) 1943.
[16] X. Xie, L. Gao, Carbon 45 (2007) 2365.
[17] R. Jiang, T. Huang, Y. Tang, J. Liu, L. Xue, J. Zhuang, A. Yu, Electrochim. Acta 54 (2009) 7173.
[18] Y. Chen, C. Liu, C. Liu, G. Lu, H. Cheng, Mater. Res. Bull. 42 (2007) 1935.
[19] Z. Fan, J. Chen, M. Wang, K. Cui, H. Zhou, Y. Kuang, Diam. Relat. Mater. 15 (2006) 1478.
[20] J. Li, I. Zhitomirsky, J. Mater. Process. Technol. 209 (2009) 3452.
[21] K.-W. Nam, C.-W. Lee, X.-Q. Yang, B.W. Cho, W.-S. Yoon, K.-B. Kim, J. Power Sources 188 (2009) 323.
[22] K. Gong, P. Yu, L. Su, S. Xiong, L. Mao, J. Phys. Chem. C 111 (2007) 1882.
[23] J. Li, Q. Yang, I. Zhitomirsky, J. Power Sources 185 (2008) 1569.
[24] T. Bordjiba, D. Bélanger, J. Electrochem. Soc. 156 (2009) A378.
[25] H. Yue, X. Huang, Y. Yang, Mater. Lett. 62 (2008) 3388.
[26] Y. Wang, A. Yuan, X. Wang, J. Solid State Electrochem. 12 (2008) 1101.
[27] S.-B. Ma, K.-W. Nam, W.-S. Yoon, X.-Q. Yang, K.-Y. Ahn, K.-H. Ohd, K.-B. Kim, J. Power Sources 178 (2008) 483.
[28] S.-B. Ma, K.-Y. Ahn, E.-S. Lee, K.-H. Oh, K.-B. Kim, Carbon 45 (2007) 375.
[29] Z. Fan, J. Chen, B. Zhang, F. Sun, B. Liu, Y. Kuang, Mater. Res. Bull. 43 (2008) 2085.
[30] S.-L. Chou, J.-Z. Wang, S.-Y. Chew, H.-K. Liu, S.-X. Dou, Electrochem. Commun. 10 (2008) 1724.
[31] A.L.M. Reddy, M.M. Shaijumon, S.R. Gowda, P.M. Ajayan, Nano Lett. 9 (3) (2009) 1002.
[32] H. Zhang, G. Cao, Z. Wang, Y. Yang, Z. Shi, Z. Gu, Nano Lett. 9 (2008) 2664.
[33] I.H. Kim, J.H. Kim, K.B. Kim, Solid-State Lett. 8 (2005) A369.
[34] Y. Zhang, X. Sun, L. Pan, H. Li, Z. Sun, C. Sun, B.K. Tay, J. Alloys Compd. 480 (2009) L17.
[35] E. Raymundo-Pinero, V. Khomenko, E. Frackowiak, F. Beguin, J. Electrochem. Soc. 152 (2005) A229.
[36] Y. Zhou, B. He, F. Zhang, H. Li, J. Solid State Electrochem. 8 (2004) 482.
[37] N. Du, H. Zhang, P. Wu, J. Yu, D. Yang, J. Phys. Chem. C 113 (2009) 17387.
[38] I.H. Kim, J.H. Kim, B.Y. Cho, Y.H. Lee, K.B. Kim, J. Electrochem. Soc. 153 (2006) A1451.
[39] Z.S. Lou, Q.W. Chen, W. Wang, Y.F. Zhang, Carbon 41 (2003) 3063.
[40] N. Pierard, A. Fonseca, Z. Konya, I. Willems, G. Van Tendeloo, J.B. Nagy, Chem. Phys. Lett. 335 (2001) 1.
[41] J.M. Ko, K.M. Kim, Mater. Chem. Phys. 114 (2009) 837.
[42] C. Lin, J.A. Ritter, B.N. Popov, J. Electrochem. Soc. 146 (1999) 3155.
[43] M. Toupin, T. Brousse, D. Bélanger, Chem. Mater. 14 (2002) 3946.
[44] Y.-C. Hsieh, K.-T. Lee, Y.-P. Lin, N.-L. Wu, S.W. Donne, J. Power Sources 177 (2008) 660.
[45] S.C. Pang, M.A. Anderson, T.W. Chapman, J. Electrochem. Soc. 147 (2000) 444.
[46] H.Y. Lee, J.B. Goodenough, J. Solid State Chem. 144 (1999) 220.
[47] H.Y. Lee, V. Manivannan, J.B.C.R. Goodenough, Acad. Sci., Ser. IIc: Chim. 13 (1999) 565.
[48] L. Cao, F. Xu, Y. Liang, H. Li, Adv. Mater. 16 (2004) 1583.